

# Efficient time-bin qubit analyzer compatible with multimode optical channels

Jeongwan Jin<sup>1,\*</sup>, Sascha Agne<sup>1</sup>, Jean-Philippe Bourgoin<sup>1</sup>, Yanbao

Zhang<sup>1</sup>, Norbert Lütkenhaus<sup>1</sup>, and Thomas Jennewein<sup>1,2†</sup>

<sup>1</sup> *Institute for Quantum Computing, Department of Physics and Astronomy,  
University of Waterloo, 200 University Ave West, Waterloo, Ontario, Canada and*

<sup>2</sup> *Quantum Information Science Program, Canadian Institute for Advanced Research, Toronto, ON, Canada*

Time-bin encoded photonic qubits are robust against decoherence in birefringent media such as optical fibers [1], which has led to many successful quantum communication demonstrations, including a Mach-Zehnder interferometer-based system [2], plug-and-play quantum key distribution (QKD) [3, 4], differential phase shift (DPS) [5] and coherent one-way (COW) [6] protocols, quantum teleportation [7], and elements of quantum repeaters [8]. Despite these successes, time-bin encoding is considered impractical for turbulent free-space or multimode fiber channels, because spatial and temporal mode distortions hinder the interference required for analysis of time-bin superposition states. Here we present an efficient time-bin qubit analyzer, assisted by passive relay optics, that matches the spatial mode of the interfering paths. Our system demonstrates interference visibility of 89%, even for strongly distorted optical input modes emerging from multimode fiber under variable angles of incidence. We measure a high level of entanglement between a time-bin qubit and a separate polarization qubit, thereby demonstrating the feasibility of time-bin based quantum communication over optical multimodal links.

Polarization-encoded photons have been preferred for most quantum communication experiments in free space [9–13] due to their robustness against atmospheric turbulence [14]. However, over long distances or when the communicating parties are in motion, it can be challenging to maintain alignment of polarization reference frames. In addition, building polarization preserving optics and telescopes is often difficult and expensive. In particular, active or adaptive optics, utilized to compensate angular fluctuations of the link in real time, may incur unavoidable polarization fluctuations [15], leading to practical challenges for polarization-based quantum communications [16].

Time-bin encoding is an alternative which has many advantages over polarization. Despite this, it has not been implemented for quantum communications over a long-distance free-space channels. This is mainly due to turbulence-induced effects on the wavefront [17] and path [18], which make it difficult to perform interferometric measurements necessary for time-bin state projection onto superposition bases. For instance, Ursin *et al.* [9] measured turbulence-induced angle of incidence (AOI) errors of up to 100  $\mu$ rad, in addition to scintillation effects. An even larger contribution may come from telescope pointing errors between communicating parties, which can be as high as  $\pm 1.04$  mrad ( $0.06^\circ$ ) for a moving platform [19]. Most importantly, these angle variances lead to distinguishable paths in unbalanced Michelson and Mach-Zehnder interferometers, which form the basis for typical time-bin qubit analyzer (TQA) implementations.

We analyze the performance reduction of a TQA with variable AOI, assuming a Michelson interferometer with path difference  $\Delta L$ , for an incident Gaussian beam with width  $\sigma^2$  incident with an angle  $\alpha$ . The angle-dependent

interference visibility follows

$$\mathcal{V}(\alpha) = \mathcal{V}_0 e^{-\left(\frac{\Delta L_0 \tan(\alpha)}{\sqrt{2}\sigma(1+\tan(\alpha))}\right)^2}, \quad (1)$$

where  $\mathcal{V}_0$  denotes the system visibility at zero angle (see Appendix). For  $\sigma = 1.49$  mm and  $\Delta L_0 = 0.60$  m, chosen to achieve a clear separation of the time bins given our detector timing jitter and channel-induced dispersion, we expect the visibility to drop to 0.70 for  $\alpha = 1.70$  mrad and  $\mathcal{V}_0 = 0.91$ . Furthermore, the relative phase between the two paths is very sensitive to the AOI, with a predicted  $\pi$ -shift per 349 nanorad input angle variation (see Appendix). The relationship Eq. (1) is verified experimentally with a single-mode beam (see Fig. 1(b)), generated by a continuous-wave (CW) laser at 776 nm. As shown in Fig. 1(c), the initial interference visibility of  $\mathcal{V}_0^{\text{single}} = 0.91 \pm 0.01$  decreases rapidly with AOI when no correction optics are implemented, as expected from Eq. (1). Next, the same laser beam is sent through a 1m-long step-index multimode fiber, thereby distorting it into a multimodal beam [20] which mimicks the effect of turbulent atmosphere (Fig. 1(d), see [9, 17] for comparison). Despite lengthy and careful alignment we are only able to obtain a maximum visibility of  $\mathcal{V}_0^{\text{multi}} = 0.16 \pm 0.01$ , which, as shown in Fig. 1(e), drops with AOI. Current solutions to this behavior include spatial-mode filtering using single-mode optical fibers, which, however, discard most of the impinging photons [21]. These observations clearly show that, given the expected angular deviations reported for free-space quantum channels, it would be technically very challenging to achieve a reliable, stable and efficient operation of time-bin qubit receiver using standard interferometers.

These interference challenges are overcome by utilizing

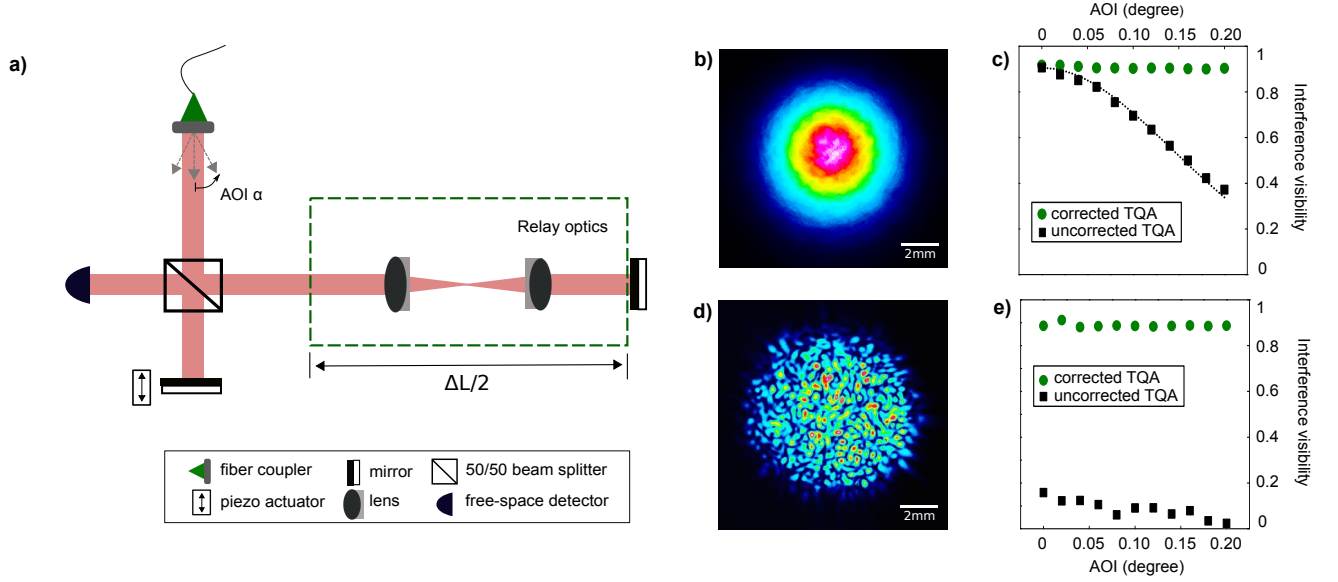


Figure 1. **A time-bin qubit analyzer (TQA).** **a)** Schematic diagram of the relay-optics-assisted TQA. Temporal separation between paths is set to  $2.0\text{ ns}$  ( $\Delta L = 0.6\text{ m}$ ). **b)** Image of the incident single-mode Gaussian beam, taken by a beam profiling camera (WinCamD-UCD12). **c)** Interference visibility for the single-mode beam with (green circles) and without (black squares) relay optics. Measured visibilities are in good agreement with theoretical prediction of Eq. (1) (dashed black line). **d)** Image of the incident multimode beam, generated by a 1-m-long step-index multimode fiber (Thorlabs M43L01). **e)** Interference visibility for the multimode beam with (green circles) and without (black squares) relay optics. Correcting with relay optics not only improves performance at higher AOI but is necessary to enable high interference visibility with a multimode beam. Uncertainties are smaller than symbol size.

relay optics in the long arm of the unbalanced Michelson interferometer, as depicted in Fig. 1(a). Effectively, the relay optics reverse differences in the evolution of the spatial mode over length  $\Delta L$  in the long arm (see Appendix). With our new TQA design, for a single-mode beam, an interference visibility of  $\mathcal{V}_{\text{avg}}^{\text{single}} = 0.91 \pm 0.01$  is obtained, which remains constant as the AOI is varied (see Fig. 1(c)). The improvement is further confirmed by measurements with a multimode beam (Fig. 1(d)) where the high visibility of  $\mathcal{V}_{\text{avg}}^{\text{multi}} = 0.89 \pm 0.01$  (Fig. 1(e)) demonstrates that the interferometer design is robust against highly distorted beams. The measured optical throughput of the interferometer is 0.74 including multimode fiber-coupling efficiency of 0.87, showing that the relay lenses faithfully symmetrize the two paths of the interferometer.

The utility of our interferometer design, as a working TQA for multimodal quantum signals, is demonstrated with the experimental setup depicted in Fig. 2. A source generates polarization-entangled photon pairs centered at 776 nm and 842 nm (see Appendix) with initial entanglement visibilities of  $\mathcal{V}_z^{\text{ref}} = 0.979 \pm 0.013$  and  $\mathcal{V}_{xy}^{\text{ref}} = 0.901 \pm 0.012$ . The 776 nm polarization qubit is converted into a time-bin qubit, resulting in the hybrid state

$$|\psi\rangle = \frac{1}{\sqrt{2}}(|H\rangle|E\rangle + |V\rangle|L\rangle), \quad (2)$$

where  $|H\rangle$  ( $|V\rangle$ ) and  $|E\rangle$  ( $|L\rangle$ ) denotes the quantum state in which the 842 nm photon is in *horizontal* (*vertical*) polarization mode and the 776 nm photon in *early* (*late*) temporal mode (see Appendix).

The 776 nm photon is sent through a 1 m-long step-index multimode fiber to artificially distort the spatial mode (see Fig. 3(a)) and the temporal mode, with a measured dispersion of about 50 ps, drastically exceeding the photon's coherence time of 3.2 ps [22], prior to entering our multimode time-bin qubit analyzer (MM-TQA). The output of the interferometer is coupled into a multimode fiber for delivery of the photons to the detector (Si-avalanche photodiode).

Verification of the MM-TQA performance is done by measuring entanglement visibilities between the polarization and time-bin qubits. Each qubit is first projected onto basis states, i.e.  $|\sigma_{\pm z}\rangle\langle\sigma_{\pm z}|$ , where  $|\sigma_{+z(-z)}\rangle$  denotes  $|H(V)\rangle$  and  $|E(L)\rangle$  for a 842 and a 776 nm photon, respectively. The coincidence counts are used to calculate a visibility, defined as  $\mathcal{V}_{\pm z} \equiv (N_{\pm z \pm z} - N_{\mp z \pm z}) / (N_{\pm z \pm z} + N_{\mp z \pm z})$ , and the average value of  $\mathcal{V}_z = (\mathcal{V}_{+z} + \mathcal{V}_{-z}) / 2 = 0.952 \pm 0.011$  is observed. Here,  $N_{ij}$  denotes the joint-detection counts between a 842 nm photon projected onto  $|\sigma_i\rangle\langle\sigma_i|$  and a 776 nm photon onto  $|\sigma_j\rangle\langle\sigma_j|$ , where  $i, j \in \{+z, -z\}$  (see Fig. 3(b)).

More important for the MM-TQA operation is the projection of the time-bin qubits onto superposition states,

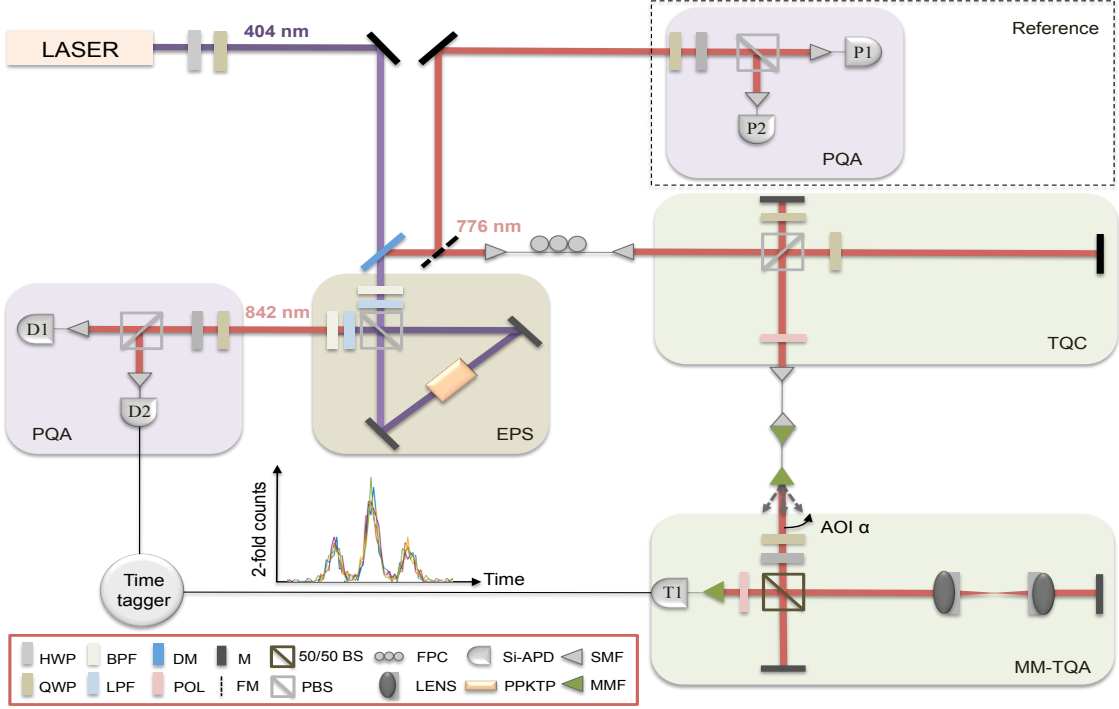


Figure 2. **Experimental setup.** The polarization-entangled photon-pair source (EPS) is described in the Appendix. For projection measurements, a 842 nm photon is directed to a polarization-qubit analyzer (PQA), consisting of a quarter-wave plate (QWP), a half-wave plate (HWP), a polarizing beam splitter (PBS), and silicon avalanche photodiodes (Si-APDs) with timing jitter of 600 ps. After reflection at a dichroic mirror (DM), by a flip mirror (FM), a 776 nm photon is sent either to a PQA or a time-bin qubit converter (TQC) followed by a multimode time-bin qubit analyzer (MM-TQA). The purpose of the PQA is to measure reference entanglement visibilities with the source of polarization entanglement, which will be compared to visibilities with polarization-time entanglement. The TQC maps the 776 nm polarization qubit onto a time-bin qubit (see Appendix). For projection measurements, the time-bin qubit, spatially and temporally distorted by a multimode fiber (MMF), is then sent to a MM-TQA whose output is coupled into a MMF before detection by a Si-APD. A polarizer (POL) removes any possible path-dependent polarization distinguishability. All detection signals are sent to a time tagger for data analysis.

i.e.  $|\sigma_{\pm\phi}\rangle\langle\sigma_{\pm\phi}|$ , where  $|\sigma_{\pm\phi}\rangle \equiv \frac{1}{\sqrt{2}}(|\sigma_{+z}\rangle \pm e^{i\phi}|\sigma_{-z}\rangle)$ . To measure the visibility, we vary the relative phase  $\phi'$  between basis states using motorized wave-plates acting on the polarization qubit. A complete scan of the phase along the xy-plane of the Bloch sphere is performed within 10 seconds, yielding the average visibility  $\mathcal{V}_{xy} = (\mathcal{V}_{+xy} + \mathcal{V}_{-xy})/2 = 0.804 \pm 0.006$  (see Fig. 3(c)).

The entanglement verification measurements are also carried out for different AOI, demonstrating that the measured visibilities (in Fig. 3(d)) are constant within experimental errors. Due to the coupling geometry of the photons into the multimode detector fiber, the photon-collection efficiency of 0.87 decreases with AOI and drops to zero at  $\pm 0.24$  degrees. However, the fact that the interference visibility is essentially invariant to variation of AOI confirms the robustness of our MM-TQA.

Without relay optics, a variance of AOI also introduces phase fluctuations of the time-bin qubit analyzer. For instance, Dixon *et al.* [23] measured an angular deflection of 400 femtorad using interferometric phase mea-

surements. From our theoretical model, we anticipate  $5\pi$ -shift with an AOI of only  $1.75 \mu\text{rad}$  ( $0.0001^\circ$ ) (see Appendix). In order to assess the phase stability of our MM-TQA with AOI, we measure expectation values, defined as  $E_\phi \equiv (N_{+\phi'} - N_{-\phi'}) / (N_{+\phi'} + N_{-\phi'})$ , for AOIs changing from  $-0.20^\circ$  to  $+0.20^\circ$  continuously over 20 seconds. As shown in Fig. 4, the measured  $E$ -values remain almost constant within experimental errors, showing that our MM-TQA prevents the AOI-caused phase fluctuations. Moreover, by performing continuous projection measurements over a half an hour, we also test the long-term stability of our passively stabilized MM-TQA and observed the measured  $E$ -values change very slowly during the measurement period (see Supplementary Information (SI)). Hence, this MM-TQA could be used for reference-frame-independent (RFI) QKD in which secret keys are extracted under slow drift of measurement bases [24–27].

The suitability of the multimode TQA for quantum communications is further substantiated by examining

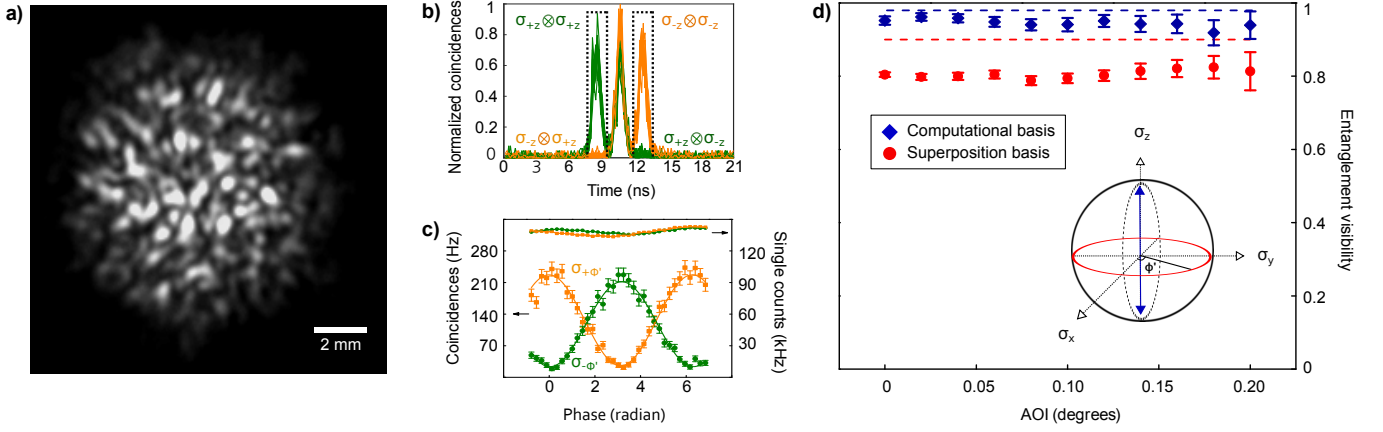


Figure 3. **Experimental results for entangled photons analyzed with the novel MM-TQA.** **a)** Spatial mode of 776 nm photons before entering the MM-TQA. The image is captured by a Hamamatsu electron multiplier (EM) CCD camera (C9100-13). **b)** Joint detections for the projection  $\sigma_{\pm z} \otimes \sigma_{\pm z}$  as a function of detection-time difference between a 776 nm and a 842 nm photon. **c)** Joint detections for the projection  $\sigma_{\pm \phi'} \otimes \sigma_{\phi}$  as a function of phase  $\phi'$  of a polarization qubit. Visibilities  $\mathcal{V}_{\pm xy}$  are obtained from sinusoidal fittings. Single counts remain essentially constant as we scan the phase. **d)** The measurement b) and c) are repeated for different AOIs. Blue diamonds are obtained from projection measurements along the computational basis (z-axis of Bloch sphere, as seen in (b)) and red circles superposition basis (xy-plane of Bloch sphere, as seen in (c)). Dashed blue and red lines are reference visibilities measured directly with the source of polarization-polarization entanglement. We maintain high entanglement visibility (close to source visibility) despite the high multimode nature of the incoming photons.

a CHSH-Bell inequality [28] from measurements on the hybrid entangled state. We prepare two bases on  $xz$ -plane of a Bloch sphere for the polarization qubit, i.e.,  $|\sigma_{z\pm x}\rangle\langle\sigma_{z\pm x}|$ . For the time-bin qubit, one basis ( $|\sigma_z\rangle\langle\sigma_z|$ ) is set deterministically, while the second one ( $|\sigma_x\rangle\langle\sigma_x|$ ) is made to drift using a heat gun, owing to the absence of active phase control in our current TQA. A search for the maximally achievable CHSH-Bell parameter is performed by scanning the second basis ( $|\sigma_\phi\rangle\langle\sigma_\phi|$ ) along the  $xy$ -plane of the time-bin states. A maximum value of  $S_{\text{exp}} = 2.42 \pm 0.05$  is found. This is in good agreement with the predicted parameter  $S_{\text{theo}} = 2.47 \pm 0.02$  calculated assuming the state described in Eq. (2) is exposed to noise modeled by an asymmetric depolarization channel (see SI).

A more rigorous verification of entanglement takes practical assumptions into account, including the photon loss in the channel and path-dependent transmission in the MM-TQA. We numerically find minimum visibilities required to detect the presence of entanglement for arbitrary  $2 \times 3$ -dimensional quantum system (see SI). Measured visibilities  $\mathcal{V}_z = 0.95 \pm 0.02$  and  $\mathcal{V}_{xy} = 0.81 \pm 0.02$  averaged over various AOIs are well above the obtained classical bound, revealing clear evidence of entanglement (see Fig. 5). Note that the obtained numerical results are valid regardless of the system efficiency and mismatched transmission between the two paths of TQA.

While theoretically  $\mathcal{V}_0 \approx 1$ , the performance of the current MM-TQA shows about  $\mathcal{V}_0 = 0.9$ , which is expected to be improved considering several approaches. First, the overlap of the spatial modes in the interfer-

ometer can be improved with careful custom design and selection of optical elements and optimization of beam diameters. Second, appropriate mode matching optics in both paths will improve the interference quality because of dispersion symmetrization at the expense of increasing complexity of the system.

In conclusion, we demonstrated a novel time-bin qubit analyzer, robust against multimode distortions on the quantum link as expected from turbulence-induced effects, i.e. wavefront distortions and path-delay fluctuations, as well as telescope pointing errors. The main benefit of our analyzer is that it is entirely based on passive optics without any active feedback systems for beam correction. Despite strong spatial and temporal distortions of the incident photon modes, we observe a robust entanglement visibility of 0.80 in the superposition bases which remains constant with variable angles of incidence. At the same time, our MM-TQA has a very high throughput efficiency of 0.74 from input to output, mainly limited by optical surface losses which can be improved. Our results open the door for implementing time-bin based quantum communication experiments over turbulent free-space and multimodal channels such as with moving platforms, including aircraft and satellites, or through non-polarization maintaining windows. Furthermore, as a quantum state receiver, the multimode time-bin qubit analyzer should also be suitable for COW, DPS, and reference-frame-independent QKD protocols.

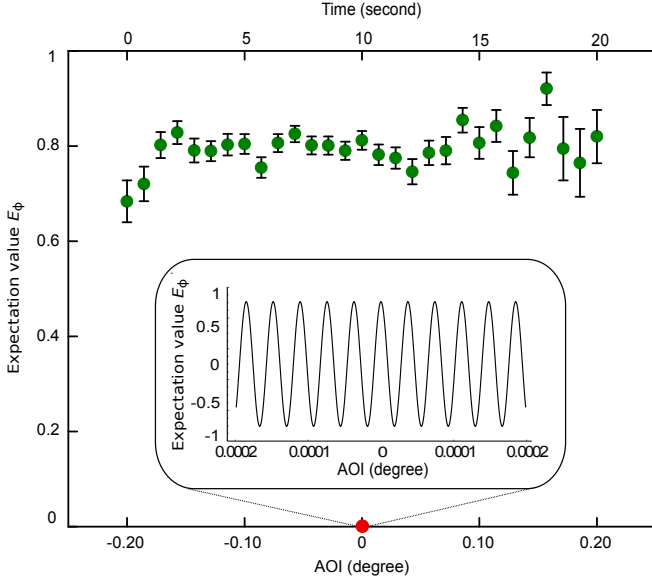


Figure 4. **Phase stability of MM-TQA** Expectation values (green circles) are measured as the AOI is continuously varied from  $-0.2^\circ$  to  $+0.2^\circ$  over 20 seconds. The inset shows the expectation value without relay optics as a function of AOI. Due to AOI-induced phase fluctuations, the value rapidly changes with AOI and thus yields an average value of zero (red circle). Measured visibility  $\mathcal{V}_{xy} = 0.80$  bounds the value  $E_\phi$ . These phase fluctuations are corrected by the relay optics, allowing a near constant expectation value.

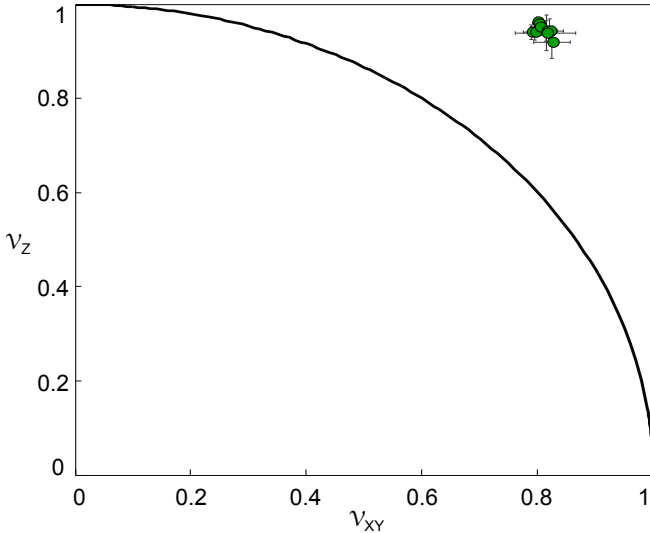


Figure 5. **Entanglement verification.** Negative Partial Transpose (NPT) criterion [29, 30] is used to obtain the required entanglement visibilities, certifying the presence of entanglement in arbitrary  $2 \times 3$ -dimensional quantum state. Our experimental results for various angles (green circles) are well above the classical bound (black line).

## APPENDIX

**Analysis of an uncorrected time-bin qubit analyzer.** Let us consider an unbalanced Michelson interferometer with long path  $L_1$  and short path  $L_2$ . The path difference for normal incidence is  $\Delta L_0 = 2(L_1 - L_2)$ . Simple ray tracing shows for an incident angle  $\alpha \neq 0$  the paths through the interferometer change with  $\alpha$  according to

$$\Delta L(\alpha) = \frac{\Delta L_0}{2} \left( \frac{1}{\cos(\alpha)} + \frac{1 - \tan(\alpha)}{\cos(\alpha) + \sin(\alpha)} \right) + \delta(\alpha) \tan \left( \alpha - \frac{\pi}{4} \right),$$

where

$$\delta(\alpha) = \frac{\Delta L_0 \tan(\alpha)}{1 + \tan(\alpha)}$$

is the lateral offset between the two rays coming from the short and long arms at the output port of the beam splitter. The angle-dependent path difference affects the photon counts in the phase-dependent basis, as the inset in Fig. 4 shows. The lateral offset reduces the interference visibility, as shown in Fig. 1. We can see this if the incoming ray is replaced by a single-mode Gaussian beam with an amplitude of  $a$  and variance  $\sigma^2$ . The intensity at the output is then given by

$$I(\delta(\alpha), \phi) = \pi a^2 \sigma^2 \left( 1 + e^{-\frac{\delta(\alpha)^2}{2\sigma^2}} \cos(\phi) \right),$$

from which we obtain the visibility in Eq. (1). Here,  $\phi$  denotes the relative phase between the paths.

**Principle of relay optics.** The relay-lens system, consisting of free space (FS) and lens (L) transmission,

$$\left\{ \begin{pmatrix} 1 & f \\ 0 & 1 \end{pmatrix}_{\text{FS}} \begin{pmatrix} 1 & 0 \\ -1/f & 1 \end{pmatrix}_{\text{L}} \begin{pmatrix} 1 & 2f \\ 0 & 1 \end{pmatrix}_{\text{FS}} \begin{pmatrix} 1 & 0 \\ -1/f & 1 \end{pmatrix}_{\text{L}} \begin{pmatrix} 1 & f \\ 0 & 1 \end{pmatrix}_{\text{FS}} \right\}^2 = \mathbb{1}$$

can be inserted into the long arm of an unbalanced Michelson interferometer (see Fig. 1(a)) in order to remove the spatial evolution caused by the path-length difference. Here,  $f$  denotes the focal length of the lenses. Note that image inversion at mirrors is excluded as this happens in both paths with no effect on the path indistinguishability.

**Source of polarization-entangled photons.** Light from a 404 nm CW laser with an average power of 6 mW pumps a periodically poled potassium titanyl phosphate (PPKTP) crystal inside a Sagnac interferometer. This generates polarization entangled photon pairs at 776 nm and 842 nm via type-II SPDC:  $|\psi\rangle = \frac{1}{\sqrt{2}}(|\text{HV}\rangle + |\text{VH}\rangle)$ ,

where H(V) denotes *horizontal (vertical)* polarization. The downconverted photons are spectrally filtered with 12 nm band-pass filters (BPF) and pump photons are removed with long-pass filters (LPFs). The ratio of coincidence-to-single counts is measured to be 0.07.

**Time-bin qubit conversion.** The 776 nm photon from the polarization-entangled photon pair is sent through a single-mode fiber (SMF) to the time-bin qubit converter (TQC). A polarization controller (FPC) ensures the faithful transmission of the polarization state. At the PBS of the TQC, the photon is either transmitted or reflected into the short or long path, respectively. To ensure both photons leave the interferometer at the desired output port, a quarter-wave plate is inserted in each path. Directly after the interferometer the photon passes through a polarizer (POL) set to an equal superposition between the polarizations. This allows, at the cost of 50 % transmission loss, to erase polarization information for each time-bin state, which completes the map  $|H\rangle \mapsto |L\rangle$  and  $|V\rangle \mapsto |E\rangle$  from polarization to time-bin state. The time-bin qubit is then coupled into a SMF with a collection efficiency of 0.67, which gives a total transmission through the TQC of 0.24.

## ACKNOWLEDGEMENTS

The authors thank Jacob Koenig, Rolf Horn, Evan Meyer-Scott, and Patrick Coles for useful discussions, and Martin Laforest for lending us the Hamamatsu EM-CCD camera. We gratefully acknowledge supports through the Office of Naval Research (ONR), the Canada Foundation for Innovation (CFI), the Ontario Research Fund (ORF), the Canadian Institute for Advanced Research (CIFAR), the Natural Sciences and Engineering Research Council of Canada (NSERC), and Industry Canada.

---

\* jeongwan.jin@uwaterloo.ca

† thomas.jennewein@uwaterloo.ca

- [1] J. Brendel, N. Gisin, W. Tittel, and H. Zbinden, Pulsed energy-time entangled twin-photon source for quantum communication, *Phys. Rev. Lett.* **82**, 2594 (1999).
- [2] P. D. Townsend, J. G. Rarity, and P. R. Tapster, *Elec. Lett.* **29**, 634 (1993).
- [3] A. Muller, T. Huttner, W. Tittel, H. Zbinden, and N. Gisin, ‘Plug and play’ systems for quantum cryptography, *Appl. Phys. Lett.* **70**, 793 (1997).
- [4] D. Stucki, N. Gisin, O. Guinnard, G. Ribordy, and H. Zbinden, Quantum key distribution over 67 km with a plug and play system, *New J. Phys.* **4**, 41 (2002).
- [5] K. Inoue, E. Waks, and Y. Yamamoto, Differential phase shift quantum key distribution. *Phys. Rev. Lett.* **89**, 037902 (2002).
- [6] D. Stucki, C. Barreiro, S. Fasel, J.-D. Gautier, O. Gay, N. Gisin, R. Thew, Y. Thoma, P. Trinkler, F. Vannel, and H. Zbinden, Continuous high speed coherent one-way quantum key distribution, *Opt. Express* **17**, 13326 (2009).
- [7] I. Marcikic, H. de Riedmatten, W. Tittel, H. Zbinden, and N. Gisin, Long-distance teleportation of qubits at telecommunication wavelengths, *Nature* **421**, 509 (2003).
- [8] E. Saglamyurek, N. Sinclair, J. Jin, J. A. Slater, D. Oblak, F. Bussi eres, M. George, R. Ricken, W. Sohler, and W. Tittel, Broadband waveguide quantum memory for entangled photons, *Nature* **469**, 512 (2011).
- [9] R. Ursin, F. Tiefenbacher, T. Schmitt-Manderbach, H. Weier, T. Scheidl, M. Lindenthal, B. Blauensteiner, T. Jennewein, J. Perdigues, P. Trojek, B.  omer, M. F urst, M. Meyenburg, J. Rarity, Z. Sodnik, C. Barbieri, H. Weinfurter, and A. Zeilinger, Entanglement-based quantum communication over 144 km, *Nat. Phys.* **3**, 481 (2007).
- [10] X.-S. Ma, T. Herbst, T. Scheidl, D. Wang, S. Kropatschek, W. Naylor, B. Wittmann, A. Mech, J. Kofler, E. Anisimova, V. Makarov, T. Jennewein, R. Ursin, and A. Zeilinger Quantum teleportation over 143 kilometres using active feed-forward, *Nature* **489**, 269 (2012).
- [11] J. Yin, J.-G. Ren, H. Lu, Y. Cao, H.-L. Yong, Y.-P. Wu, C. Liu, S.-K. Liao, F. Zhou, Y. Jiang, X.-D. Cai, P. Xu, G.-S. Pan, J.-J. Jia, Y.-M. Huang, H. Yin, J.-Y. Wang, Y.-A. Chen, C.-Z. Peng, and J.-W. Pan, Quantum teleportation and entanglement distribution over 100-kilometre free-space channels, *Nature* **488**, 185 (2012).
- [12] S. Nauerth, F. Moll, M. Rau, C. Fuchs, J. Horwath, S. Frick, and H. Weinfurter, Air-to-ground quantum communication, *Nat. Photon.* **7**, 382 (2013).
- [13] T. Herbst, T. Scheidl, M. Fink, J. Handsteiner, B. Wittmann, R. Ursin, and A. Zeilinger, Teleportation of entanglement over 143 km, *arXiv:1403.0009* (2014).
- [14] D. H ohn, Depolarization of a laser beam at 6328 Å due to atmospheric transmission, *App. Opt.* **8**, 367 (1969).
- [15] M. Jofre, G. Anzolin, F. Steinlechner, N. Oliverio, J. P. Torres, V. Pruneri, and M. W. Mitchell, Fast beam steering with full polarization control using a galvanometric optical scanner and polarization controller, *Opt. Express* **20**, 12247 (2012).
- [16] C. Bonato, M. Aspelmeyer, T. Jennewein, C. Pernechele, P. Villoresi, and A. Zeilinger, Influence of satellite motion on polarization qubits in a space-earth quantum communication link, *Opt. Express* **14**, 10050 (2006).
- [17] D. L. Fried and J. L. Vaughn, Branch cuts in the phase function, *App. Opt.* **31**, 2865 (1992).
- [18] L. Kral, I. Prochazka, K. Hamal, Optical signal path delay fluctuations caused by atmospheric turbulence, *Opt. Lett.* **30**, 1767 (2006).
- [19] J. -P. Bourgoin, B. L. Higgins, N. Gigov, C. Holloway, C. J. Pugh, S. Kaiser, M. Cranmer, and T. Jennewein, Free-space quantum key distribution to a moving receiver, *arXiv:1505.00292* (2015).
- [20] I. N. Papadopoulos, S. Farahi, C. Moser, and D. Psaltis, Focusing and scanning light through a multimode optical fiber using digital phase conjugation, *Opt. Express* **20**, 10583 (2012).
- [21] H. Takenaka, M. Toyoshima, and Y. Takayama, Experimental verification of fiber-coupling efficiency for satellite-to-ground atmospheric laser downlinks, *Opt. Express* **20**,

- 15301 (2012).
- [22] D. R. Hamel, Realization of novel entangled photon sources using periodically poled materials, M.Sc. thesis, University of Waterloo, <https://uwspace.uwaterloo.ca/handle/10012/5575> (2010).
  - [23] P. B. Dixon, D. J. Starling, A. N. Jordan, and J. C. Howell, Ultrasensitive beam deflection measurement via interferometric weak value amplification, *Phys. Rev. Lett.* **102**, 173601 (2009).
  - [24] A. Laing, V. Scarani, J. G. Rarity, and J. L. O'Brien, Reference-frame-independent quantum key distribution, *Phys. Rev. A* **82**, 012304 (2010).
  - [25] L. P. Thinh, L. Sheridan, and V. Scarani, Tomographic quantum cryptography protocols are reference frame independent, *Int. Journal. of Quantum. Info.* **10**, 1250035 (2012).
  - [26] P. Zhang, K. Aungkunsiri, E. Martin-López, J. Wabnig, M. Lobino, R. W. Nock, J. Munns, D. Bonneau, P. Jiang, H. W. Li, A. Laing, J. G. Rarity, A. O. Niskanen, M. G. Thompson, and J. L. O'Brien, Reference-frame-independent quantum-key-distribution server with a telecom tether for an on-chip client, *Phys. Rev. Lett.* **112** 130501 (2014).
  - [27] W.-Y. Liang, S. Wang, H.-W. Li, Z. -Q. Yin, W. Chen, Y. Yao, J.-Z. Huang, G.-C. Guo, and Z.-F. Han, Proof-of-principle experiment of reference-frame-independent quantum key distribution with phase coding, *Sci. Rep.* **4**, 3617 (2014).
  - [28] J. F. Clauser, M. A. Horne, A. Shimony, and R. A. Holt, Proposed experiment to test local hidden-variable theories, *Phys. Rev. Lett.* **23**, 880 (1969).
  - [29] A. Peres, Separability criterion for density matrices, *Phys. Rev. Lett.* **77**, 1413 (1996).
  - [30] M. Horodecki, P. Horodecki, and R. Horodecki, Separability of mixed states: necessary and sufficient conditions, *Phys. Lett. A* **223**, 1 (1996).



## SUPPLEMENTARY INFORMATION

### A. Estimation of CHSH-Bell parameter

The non-classicality of time-polarization entanglement is bounded with an estimate of the Bell-CHSH inequality violation [1]. Despite the absence of an active phase control, required to set measurement bases for the time-bin qubit deterministically, we search for the maximally obtainable violation by varying the measurement basis. More specifically, we first set the measurement basis for the polarization qubit to  $A_1 \equiv |\sigma_{z+x}\rangle\langle\sigma_{z+x}|$  using wave plates, and slowly and continuously change the path-length difference of the multimode time-bin qubit analyzer (MM-TQA) by externally heating it. This allows us to scan projection measurements for the time-bin qubit in the superposition bases. Fig. 6(a) shows coincidences between a polarization qubit (two detectors, i.e. D1 and D2) and a time-bin qubit (three temporal modes). Detections in the *early/late* bin (*middle* bin) corresponds to a projection of the time-bin qubit onto  $B_1 \equiv |\sigma_z\rangle\langle\sigma_z|$  ( $B_2 \equiv |\sigma_\phi\rangle\langle\sigma_\phi|$ ). Owing to the absence of the second output of the TQA, we consider all possible expectation values  $E(A_i, B_j)$  between any two points in time, i.e.  $t_1$  and  $t_2$  (see Fig. 6(b)), which is defined as

$$E(A_i, B_j) = \frac{N_{ij}^{++} + N_{ij}^{--} - N_{ij}^{+-} - N_{ij}^{-+}}{N_{ij}^{++} + N_{ij}^{--} + N_{ij}^{+-} + N_{ij}^{-+}}, \quad (3)$$

Here,  $N_{ij}$  are the coincidence counts for the projections  $A_i \otimes B_j$ , where  $i, j \in \{1, 2\}$  and superscript(+, -) denotes two outcomes of the projection measurement. Among all the computed expectation values, we find the absolute maximum expectation value. We then change the measurement basis for the polarization qubit to  $A_2 \equiv |\sigma_{z-x}\rangle\langle\sigma_{z-x}|$  and repeat the procedure. Finally, we compute the CHSH-Bell inequality parameter

$$S = |E(A_1, B_1) - E(A_1, B_2) + E(A_2, B_1) + E(A_2, B_2)| \quad (4)$$

and find the value of  $S_{\text{exp}} = 2.42 \pm 0.05$ , which is clearly above classical bound  $S=2$ . To see whether this value agrees with the measured visibilities, we model the two-qubit state with noise, described by an asymmetric depolarization channel, on a time-bin qubit. The output state is then described by

$$\rho_{\text{out}} = (1 - \sum_{j=x,y,z} p_j) |\psi\rangle\langle\psi| + \sum_{j=x,y,z} p_j (\mathbb{1} \otimes \sigma_j) |\psi\rangle\langle\psi| (\mathbb{1} \otimes \sigma_j), \quad (5)$$

where  $p_j (j=x,y,z)$  and  $\sigma_j$  are the depolarization probability and single-qubit Pauli operator along the channel  $j$ , respectively. Here,  $|\psi\rangle$  denotes the input state, described in Eq. (2) of the main text. Assuming unbiased depolarizations in the superposition bases, i.e.  $(p_x = p_y) \equiv p_{xy}$ , we calculate expectation values  $E(A_i, B_j) = \text{Tr}(\rho_{\text{out}} A_i \otimes B_j)$  for given measurement bases. Using the definition of visibility, we further represent the CHSH-Bell parameter  $S_{\text{theo}} = \sqrt{2}(\mathcal{V}_z + \mathcal{V}_{xy})$  as a function of entanglement visibilities. We find  $S_{\text{theo}} = 2.47 \pm 0.02$  is in accordance with our measured value  $S_{\text{exp}} = 2.42 \pm 0.05$ .

### B. Long-term phase stability of the MM-TQA

Our multimode time-bin qubit analyzer is passively stabilized by enclosing it with black hardboard. In order to assess the phase stability of the MM-TQA, we perform joint-projection measurement onto the superposition bases over a half an hour. The time-bin qubit is projected onto a  $|\sigma_\phi\rangle\langle\sigma_\phi|$  and the polarization qubit alternatively between  $|\sigma_{\phi'}\rangle\langle\sigma_{\phi'}|$  or  $|\sigma_{\phi'+\pi/2}\rangle\langle\sigma_{\phi'+\pi/2}|$ . This allows us to calculate the expectation values, defined as  $E_{\phi',\phi} \equiv (N_{+\phi'\phi} - N_{-\phi'\phi}) / (N_{+\phi'\phi} + N_{-\phi'\phi})$ , where  $N_{ij}$  denotes joint-detection counts when a 842 nm photon is projected onto  $|\sigma_i\rangle\langle\sigma_i|$  and a 776 nm photon onto  $|\sigma_j\rangle\langle\sigma_j|$ . As shown in Fig. 7, the average expectation value  $\sqrt{E_{\phi',\phi}^2 + E_{\phi'+\pi/2,\phi}^2}$  remains always higher than 0.65, which is well above the required value  $\mathcal{V}_{xy}$  for verifying entanglement, given entanglement visibility  $\mathcal{V}_z = 0.952$  (see Fig. 5 in the main text).

### C. Entanglement verification

As entanglement is fundamentally important and an effective distribution of entanglement is a necessary condition for secure QKD [2], we need to verify whether or not entanglement is present in our experiment. This is especially important in the absence of a complete security analysis of a QKD implementation. We assume that the spontaneous parametric down-conversion process generates a pair of photons with negligible multiple-photon-pairs event. Each photon is a polarization qubit and the pair of photons is potentially entangled. By detecting one photon in the pair, we can herald the generation of the second photon. After the conversion from polarization qubit to time-bin qubit, the second one is transmitted to the MM-TQA. Suppose that Alice holds the polarization qubit while Bob holds the time-bin qubit. To include conversion and transmission losses of the time-bin qubit, we enlarge the dimension of Bob's system from 2 to 3 by adding a dimension corresponding to no photon arriving at Bob. Hence, the final state  $\rho$  shared by Alice and Bob is a  $2 \times 3$ -dimensional state. We need to verify whether or



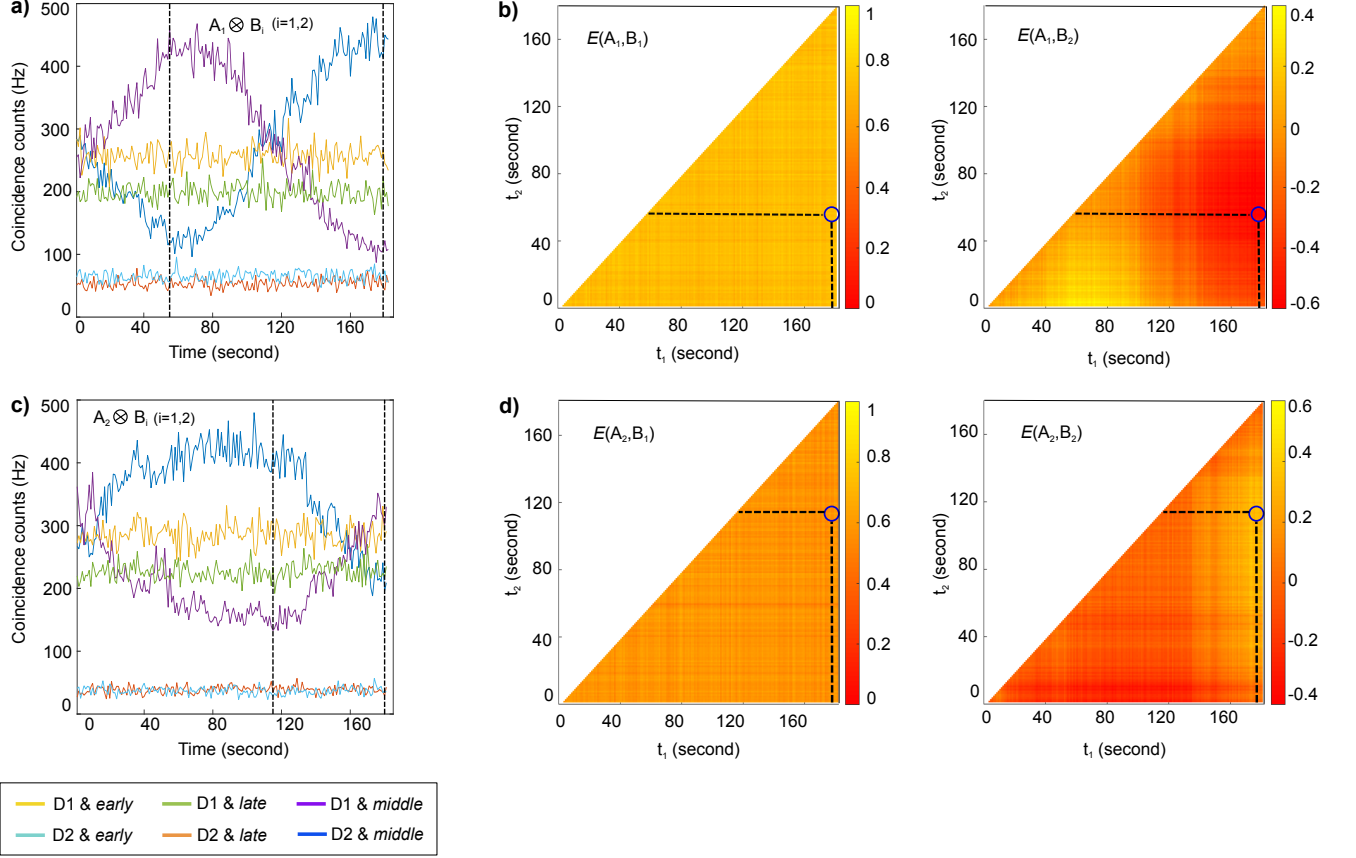


Figure 6. **Estimation of the CHSH-Bell parameter.** (a) Yellow and light blue lines are coincidences from joint projections  $\sigma_{z+x} \otimes \sigma_{+z}$  (early temporal bin), green and orange lines from  $\sigma_{z+x} \otimes \sigma_{-z}$  (late temporal bin), and purple and blue lines from  $\sigma_{z+x} \otimes \sigma_{\phi}$  (middle temporal bin). Black dashed lines are times at which maximal expectation values are extracted. (b) Surface plot of calculated expectation values for the projections in (a). (c) Yellow and light blue lines are coincidences from joint projection  $\sigma_{z-x} \otimes \sigma_{+z}$ , green and orange lines from  $\sigma_{z-x} \otimes \sigma_{-z}$ , and purple and blue lines from  $\sigma_{z-x} \otimes \sigma_{\phi}$ . Black dashed lines are times at which maximal expectation values are extracted. (d) Surface plot of calculated expectation values for the projection measurements in (c). The Bell-CHSH parameter is calculated using the maximum expectation values. The measurement duration is chosen arbitrarily and yields a violation of the inequality of  $2.42 \pm 0.05$ .

not the state  $\rho$  is entangled using only the measurement results  $\mathcal{V}_z = 0.952 \pm 0.011$  and  $\mathcal{V}_{xy} = 0.804 \pm 0.006$  without further assumptions on the state. Since the measurements of Alice and Bob are block-diagonal with respect to the subspaces of total photon number, as we will show below in Eq. (6) and (7), we can also assume without loss of generality that the state  $\rho$  shows the same structure. This follows from the fact that the measurement structure allows us to assume that a quantum non-demolition

measurement of the total photon number is executed before the actual measurement itself.

In order to verify entanglement, we need to know how to accurately describe the measurements on the polarization qubit and on the time-bin qubit. For the polarization qubit, we measure it in the *horizontal/vertical* or *diagonal/anti-diagonal* basis, i.e. along the  $z$ - or  $x$ -axis in the Bloch sphere. In the *horizontal/vertical* basis, these measurements are represented as

$$M_H = \begin{bmatrix} 1 & 0 \\ 0 & 0 \end{bmatrix}, M_V = \begin{bmatrix} 0 & 0 \\ 0 & 1 \end{bmatrix}, M_D = \frac{1}{2} \begin{bmatrix} 1 & 1 \\ 1 & 1 \end{bmatrix}, \text{ and } M_A = \frac{1}{2} \begin{bmatrix} 1 & -1 \\ -1 & 1 \end{bmatrix}, \quad (6)$$

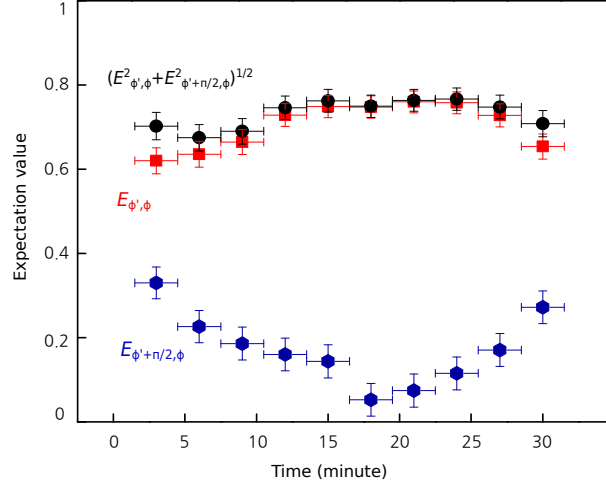


Figure 7. **Long-term phase stability of our multimode time-bin qubit analyzer.** Red squares are expectation values for projection measurements  $\sigma_{\phi'} \otimes \sigma_{\phi}$  ( $E_{\phi',\phi}$ ) and blue hexagons for  $\sigma_{\phi'+\pi/2} \otimes \sigma_{\phi}$  ( $E_{\phi'+\pi/2,\phi}$ ). Each measurement is averaged over 3 minutes. Black circles are average expectation values  $\sqrt{E_{\phi',\phi}^2 + E_{\phi'+\pi/2,\phi}^2}$ . The phase drifts slowly, on the order of  $\pi/2$  over an half an hour, showing the stability of our MM-TQA. The average expectation value is always higher than the required expectation value for entanglement verification.

where the subscript indicates measurement outcome, and H, V, D, or A denotes the *horizontal*, *vertical*, *diagonal*, or *anti-diagonal* polarization. On the other side, for the time-bin qubit, the photon loss in the long path or the short path of the MM-TQA could be different from each other. Hence, the operators corresponding to measurement of the time-bin qubit in the *early/late*-time basis or

in the superposition bases could deviate from the ideal case. Without loss of generality, we can choose the relative phase between the *early*-time and *late*-time basis states in the superposition basis to be zero. Therefore, in the basis where the basis states are no photon, one photon in the *early* bin and one photon in the *late* bin, these measurements can be written as

$$M_E = \frac{1}{4} \begin{bmatrix} 0 & 0 & 0 \\ 0 & \eta_s & 0 \\ 0 & 0 & 0 \end{bmatrix}, M_L = \frac{1}{4} \begin{bmatrix} 0 & 0 & 0 \\ 0 & 0 & 0 \\ 0 & 0 & \eta_l \end{bmatrix}, M_X = \frac{1}{4} \begin{bmatrix} 0 & 0 & 0 \\ 0 & \eta_l & \sqrt{\eta_l \eta_s} \\ 0 & \sqrt{\eta_l \eta_s} & \eta_s \end{bmatrix}, \text{ and} \\ M_{\emptyset} = I_{3 \times 3} - M_E - M_L - M_X, \quad (7)$$

where the subscript E, L, X, or  $\emptyset$  means that the measurement outcome is *early* time, *late* time, the superposition of the *early* time and *late* time, or no detection, respectively. No-detection events are due to detection inefficiency and the absence of the second output in the MM-TQA. In Eq. (7),  $\eta_l$  or  $\eta_s$  is the respective transmission efficiency in the long path or the short path of the MM-TQA. Note that in our experiment  $\eta_l$  and  $\eta_s$  are very close to each other.

After knowing the description of Alice's and Bob's joint state  $\rho$  and also that of their measurements, we can verify entanglement by the negative partial-transpose (NPT) criterion [3]. The NPT criterion is used because this criterion is satisfied if and only if a state is entangled, given the state is  $2 \times 2$ - or  $2 \times 3$ -dimensional [4]. The NPT criterion has been applied to verify entanglement in QKD systems, such as in [5]. Explicitly, we verify entanglement by solving the following semi-definite program (SDP):

find  
subject to

$$\begin{aligned}
& \rho \\
& \rho \geq 0 \\
& \text{Tr}(\rho) = 1 \\
& \rho^\Gamma \geq 0 \\
& \text{Tr}[\rho(M_H \otimes M_E - M_V \otimes M_E)] = \mathcal{V}_{+z} \text{Tr}[\rho(M_H \otimes M_E + M_V \otimes M_E)] \\
& \text{Tr}[\rho(M_V \otimes M_L - M_H \otimes M_L)] = \mathcal{V}_{-z} \text{Tr}[\rho(M_V \otimes M_L + M_H \otimes M_L)] \\
& \text{Tr}[\rho(M_D \otimes M_X - M_A \otimes M_X)] = \mathcal{V}_{xy} \text{Tr}[\rho(M_D \otimes M_X + M_A \otimes M_X)],
\end{aligned} \tag{8}$$

where  $\Gamma$  is the partial-transpose operation on a subsystem, such as on the polarization-qubit subsystem, and  $\otimes$  denotes the tensor product. Note that, we formulate the last three constraints according to the measured visibilities. The first two of them are based on entanglement visibilities  $\mathcal{V}_{+z}$  and  $\mathcal{V}_{-z}$  conditioned on measurement outcomes of the time-bin qubit being early time and late time, respectively. The last constraint is based on entanglement visibility  $\mathcal{V}_{xy}$ , where the time-bin qubit comes out in the *middle* bin. Since the MM-TQA has only one output, we cannot differentiate the case when the photon comes out from the second output if this output exists from the case when the photon is lost over the transmission. Hence, we cannot formulate two constraints based on  $\mathcal{V}_{xy}$ .

In our experiment, we verified that within experimental errors the visibilities  $\mathcal{V}_{+z} = \mathcal{V}_{-z}$ . So, for solving the SDP program in Eq. (8) we set  $\mathcal{V}_{+z} = \mathcal{V}_{-z} = \mathcal{V}_z$ . Using the measured results  $\mathcal{V}_z = 0.952$  and  $\mathcal{V}_{xy} = 0.804$ , the SDP program in Eq. (8) is not feasible, signifying that the state  $\rho$  must be entangled. Furthermore, by numerically checking over which values of  $\mathcal{V}_z$  and  $\mathcal{V}_{xy}$  the SDP program in Eq. (8) is not feasible, we are able to upper bound the required visibilities  $\mathcal{V}_z$  and  $\mathcal{V}_{xy}$  in order to certify the presence of entanglement in the system. The numerical results are shown in Fig. 5 of the main text. From this figure, one can see that our visibility result at any observed incident angle witnesses entanglement with high confidence. Finally, we would like to note two

points. First, the constraints considered in Eq. (8) are independent of the transmission or conversion loss of the photon arriving at the MM-TQA, and even independent of the common photon loss in the two different paths of the MM-TQA. Therefore, the upper bounds on the visibilities  $\mathcal{V}_z$  and  $\mathcal{V}_{xy}$  obtained for verifying entanglement are independent of all of these different losses. Second, we numerically verified that the classical boundary, as shown in Fig. 5 of the main text, is even independent of the relative loss between the two paths of the MM-TQA.

---

\* jeongwan.jin@uwaterloo.ca

† thomas.jennewein@uwaterloo.ca

- [1] J. F. Clauser, M. A. Horne, A. Shimony, and R. A. Holt, Proposed experiment to test local hidden-variable theories, *Phys. Rev. Lett.* **23**, 880 (1969).
- [2] M. Curty, M. Lewenstein, and N. Lütkenhaus, Entanglement as a precondition for secure quantum key distribution, *Phys. Rev. Lett.* **92**, 217903 (2004).
- [3] A. Peres, Separability criterion for density matrices, *Phys. Rev. Lett.* **77**, 1413 (1996).
- [4] M. Horodecki, P. Horodecki, R. Horodecki, Separability of mixed states: necessary and sufficient conditions, *Phys. Lett. A* **223**, 1 (1996).
- [5] M. Curty and T. Moroder, Single-photon quantum key distribution in the presence of loss, *Phys. Rev. A* **75**, 052336 (2007).